Single-cell multiomics reveals the oscillatory dynamics of mRNA metabolism and chromatin accessibility during the cell cycle

Maulik K Nariya, David Santiago-Algarra, Olivier Tassy, Marie Cerciat, Tao Ye, Andrea Riba, Nacho Molina

Cell Reports

Article

Single-cell multiomics reveals the oscillatory dynamics of mRNA metabolism and chromatin accessibility during the cell cycle

Graphical abstract

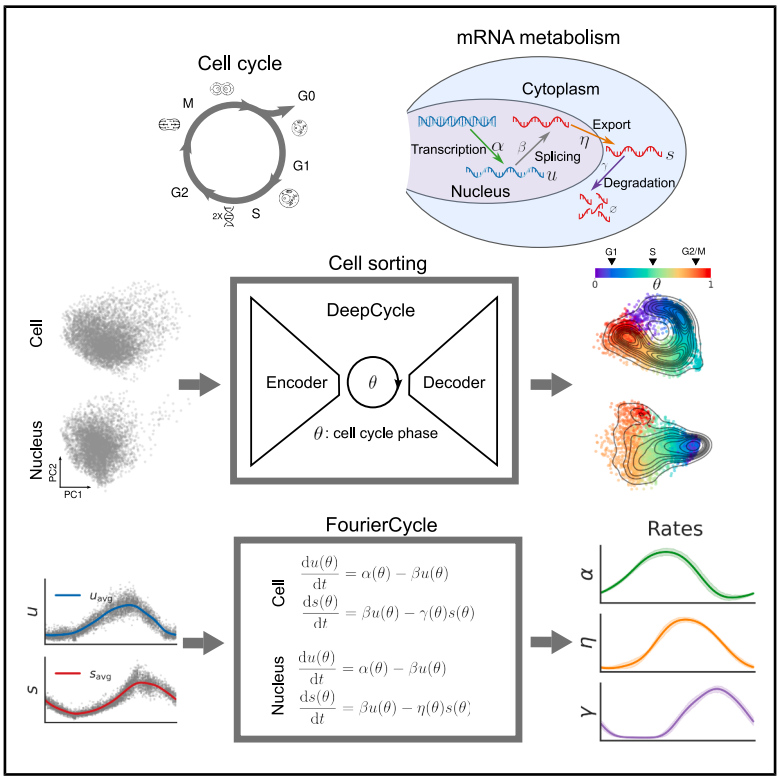

Highlights

- FourierCycle infers gene-specific rates of mRNA metabolism using multiome data and modeling
- mRNA synthesis, export, and decay show gene-specific waves during the cell cycle
- Post-transcriptional regulation strongly shapes mRNA levels across the cell cycle
- Chromatin and TF footprint dynamics reveal key regulators of gene expression dynamics

Authors

Maulik K. Nariya, David Santiago-Algarra, Olivier Tassy, Marie Cerciat, Tao Ye, Andrea Riba, Nacho Molina

Correspondence

nariyam@igbmc.fr (M.K.N.), molinan@igbmc.fr (N.M.)

In brief

Nariya et al. use deep learning and biophysical modeling on single-cell multiome data to reveal genome-wide oscillatory gene expression during the cell cycle in mouse embryonic stem cells, modeling mRNA dynamics and chromatin accessibility to provide a detailed, cell-cycle-dependent view of transcription, degradation, and nuclear export processes.

Nariya et al., 2025, Cell Reports *44*, 116089
August 26, 2025
https://doi.org/10.1016/j.celrep.2025.116089

CellPress

Cell Reports

CellPress
OPEN ACCESS

Article

Single-cell multiomics reveals the oscillatory dynamics of mRNA metabolism and chromatin accessibility during the cell cycle

Maulik K. Nariya,[1,2,3,4,6,*] David Santiago-Algarra,[1,2,3,4] Olivier Tassy,[1,2,3,4] Marie Cerciat,[1,2,3,4] Tao Ye,[1,2,3,4] Andrea Riba,[1,2,3,4,5] and Nacho Molina[1,2,3,4,7,*]

[1]Institut de Génétique et de Biologie Moléculaire et Cellulaire (IGBMC), Illkirch, France
[2]Centre National de la Recherche Scientifique (CNRS), UMR 7104, Illkirch, France
[3]Institut National de Santé et de Recherche Médicale (ISERM), UMR-S 1258, Illkirch, France
[4]Université de Strasbourg, IGBMC UMR 7104-UMR-S 1258, Illkirch, France
[5]Present address: Capgemini, Turin, Italy
[6]Senior author
[7]Lead contact
*Correspondence: nariyam@igbmc.fr (M.K.N.), molinan@igbmc.fr (N.M.)
https://doi.org/10.1016/j.celrep.2025.116089

SUMMARY

The cell cycle is a tightly regulated process that requires precise temporal expression of thousands of cell-cycle-dependent genes. However, the genome-wide dynamics of mRNA metabolism throughout the cell cycle remain uncharacterized. Here, we combined single-cell multiome sequencing, biophysical modeling, and deep learning to quantify rates of mRNA transcription, splicing, nuclear export, and degradation. Our approach revealed that both transcriptional and post-transcriptional processes exhibit distinct oscillatory waves at specific cell cycle phases, with post-transcriptional regulation playing a prominent role in shaping mRNA accumulation. We also observed dynamic changes in chromatin accessibility and transcription factor binding footprints, identifying key regulators underlying the oscillatory dynamics of mRNA. Taken together, the results of our approach uncovered a high-resolution map of RNA metabolism dynamics and chromatin accessibility, offering new insights into the temporal control of gene expression in proliferating cells.

INTRODUCTION

The cell cycle is a highly regulated process that ensures the accurate replication and transmission of genetic information from one generation of cells to the next. It is a fundamental biological process and plays a crucial role in the development, growth, and maintenance of all living organisms, and its dysregulation can lead to a number of pathologies, such as autoimmune diseases, neurodegenerative diseases, and cancer.[1–8] In general, the cell cycle proceeds through four phases: G1, a period when the cell duplicates essential cellular components; S, a period of DNA duplication; G2, when organelles and proteins for cell division develop; and M phase, which completes the process.[1] Unimpeded progression through the cell cycle requires precise and regulated deployment of hundreds of proteins and thus represents one of the most complex and tightly spatiotemporally controlled processes in biology.[1–8] The levels of these proteins are, in part, controlled by periodic expression of their mRNAs during the cell cycle, often observed as waves of gene expression.[9–11] However, studies of the mRNAs and how they emerge, change, and dissipate during different phases of the cell cycle at high temporal resolution have remained technically challenging.

Recently, RNA velocity, i.e., the time derivative of the gene expression state, was introduced as a framework to obtain the systems-level dynamics of gene expression from static snapshots of transcriptional states measured at single-cell resolution.[12–15] RNA velocity depends on the four main steps in mRNA metabolism: (1) transcription, which generates pre-mRNA (unspliced mRNA), (2) pre-mRNA splicing to obtain mature mRNA (spliced mRNA), (3) the mature mRNA export into the cytoplasm for protein synthesis, and (4) mRNA degradation. In this context, measuring unspliced and spliced mRNA levels in cells at single-cell resolution can provide a dynamical picture of cellular processes.[12–15] However, this approach does not provide a way to gain insights into the dynamics of the cell cycle. Furthermore, although computational tools such as Cyclum and Revelio have been developed to infer the cell cycle phase based on single-cell RNA sequencing (scRNA-seq) data, these methods do not take into account RNA velocity and offer no insight into RNA metabolism.[10,11] To begin to address these limitations, we recently developed DeepCycle, a deep learning tool that uses scRNA-seq to map the gene expression profiles to a continuous latent variable, θ, representing the cell cycle phase.[16] We used DeepCycle to study dynamics of gene expression at high temporal resolution in embryonic and

somatic cells, revealing major waves of RNA accumulation during the cell cycle and identifying key transcriptional regulators involved in cell cycle progression. This led to the question, how are the processes that govern RNA accumulation, such as transcription, nuclear export, splicing, and degradation, temporally regulated during the cell cycle on a genome-wide scale?

Here, we address this by combining scRNA-seq, single-nucleus multiome sequencing, DeepCycle, and biophysical model construction. Our model, which we call FourierCycle,[17] predicts that the cell cycle depends on transcription, nuclear export, and degradation rates for every gene, revealing waves of transcriptional and post-transcriptional regulation during the cell cycle. Furthermore, our method allowed us to investigate changes in chromatin accessibility at the gene level and their potential connection to transcription. Remarkably, we identified key transcription factors (TFs) and the dynamics of their binding activities during the cell cycle by examining changes in chromatin accessibility footprints near their binding sites. In summary, we developed a framework that combines state-of-the-art sequencing technologies with deep learning and biophysical modeling to uncover a global picture of transcriptional and post-transcriptional regulation of mRNA accumulation and chromatin accessibility dynamics throughout the cell cycle.

RESULTS

DeepCycle sorts single cells and single nuclei according to their cell cycle progression

The mouse embryonic stem cells (mESCs) were cultured in serum-supplemented 2i + LIF (details provided in STAR Methods). This treatment promotes the maintenance of a self-renewal cell state, reducing heterogeneous expression of pluripotency factors and spontaneous differentiation, thereby generating an asynchronous population of proliferating cells.[18,19] The serum supplementation improved cell viability and gave more homogeneous colonies. The results of our findings must be interpreted with regard to these culture conditions. We previously performed scRNA-seq to obtain the transcriptomes of whole mESCs.[11] To complement this dataset with nuclear RNA expression and chromatin accessibility information, we employed the multiome protocol that involved simultaneously performing single-nucleus RNA sequencing (snRNA-seq) and single-nucleus assay for transposase-accessible chromatin using sequencing (snATAC-seq) on the same cells.[20] We profiled around 5,000 cells in each experiment at high sequencing depth, revealing the gene expression of roughly 12,000 genes. To obtain an overall view and comparison between the single-cell and single-nucleus data, we calculated the average reads of unspliced and spliced RNA across genes and across cells (or nuclei) (Figures 1A–1D). Comparing the unspliced and spliced reads in the cell with ones in the nucleus revealed a strong correlation between the mRNA reads obtained from the nuclear data and those obtained from the cell data ($r = 0.86$ for unspliced and 0.78 for spliced), suggesting a high degree of coherence in the measurements (see Figure S1 for corresponding figures for replicate 2). The points in the scatterplot in Figure 1C are equally distributed across the $x = y$ line, suggesting that most of the unspliced molecules of the cell reside in the nucleus, whereas most of the points in the scatterplot in 2D are below the $x = y$ line, suggesting that most of the spliced molecules are present in the cytoplasm of the cell, in agreement with what we expected to see.

Next, we used DeepCycle and both the scRNA-seq and snRNA-seq data from mESCs and determined the cell cycle phase of each cell and nucleus. Our approach effectively revealed the cell cycle manifold embedded in gene expression space, as depicted in the projection onto the two main principal components (PCs) for the cell and the nucleus (Figures 1E and 1F). We observed that for the single-cell data, the cells are accurately positioned along the dynamic cycling trajectory and distinguishable based on their progression through the cell cycle (Figure 1E). For the single nuclei, although the cell cycle manifold may not appear to be cyclic, the nuclei cluster well, according to their progression through the cell cycle in the correct order (Figure 1F). Note that cells with high expression of ribosomal protein-coding genes appear as extreme outliers in the PC space and were omitted in the principal-component analysis (PCA) plot for the sake of visualization (see Figures S1A and S1B). The number of unique molecular identifiers (UMIs),[21,22] which can be interpreted as the total mRNA content of the cell, shows a 2-fold change as the cells progress through the estimated cell cycle phase (Figure 1G). This is the expected behavior, assuming that the concentration of mRNA remains constant during the cell cycle.[23] Importantly, the total mRNA content within the nucleus also exhibits a similar 2-fold increase as observed in the whole cell during the cell cycle (Figure 1H). Note that we use this to determine the M/G1 phase transition (see Figure S2 and STAR Methods section for the details) Lastly, expression dynamics of the unspliced and spliced reads for cyclin B1 (*Ccnb1*), a crucial regulator of the G2/M transition during the cell cycle,[24,25] showed gene-specific dynamics of unspliced and spliced levels of mRNA in the cell and the nucleus (Figures 1I and 1J). Note, since we use the same model system and culture conditions as in Riba et al., the transition boundaries for G1/S and S/G2 were borrowed from this work.[11] We observed that the unspliced and spliced RNA nuclear levels of *Ccnb1* mirror the dynamics observed in the entire cell. See Figure S1 for the corresponding plots in Figure 1 for replicate 2.

In summary, we obtained unique scRNA-seq and snRNA-seq datasets at a high sequencing depth and showed that DeepCycle accurately assigns a continuous phase to both single cells and single nuclei, indicating their progression through the cell cycle.

Kinetic modeling reveals cell-cycle-dependent mRNA transcription and degradation rates

DeepCycle reveals oscillatory patterns in mRNA accumulation throughout the cell cycle, prompting an investigation into the underlying processes of mRNA metabolism responsible for these dynamics. To address this question, we developed FourierCycle, a biophysical model of mRNA metabolism. As mentioned earlier, the key steps involved in mRNA metabolism include transcription, splicing, nuclear export, and degradation. These processes were modeled using a system of coupled differential equations with periodic functions to capture cell-cycle-dependent rates. We derived a pseudo-analytical solution

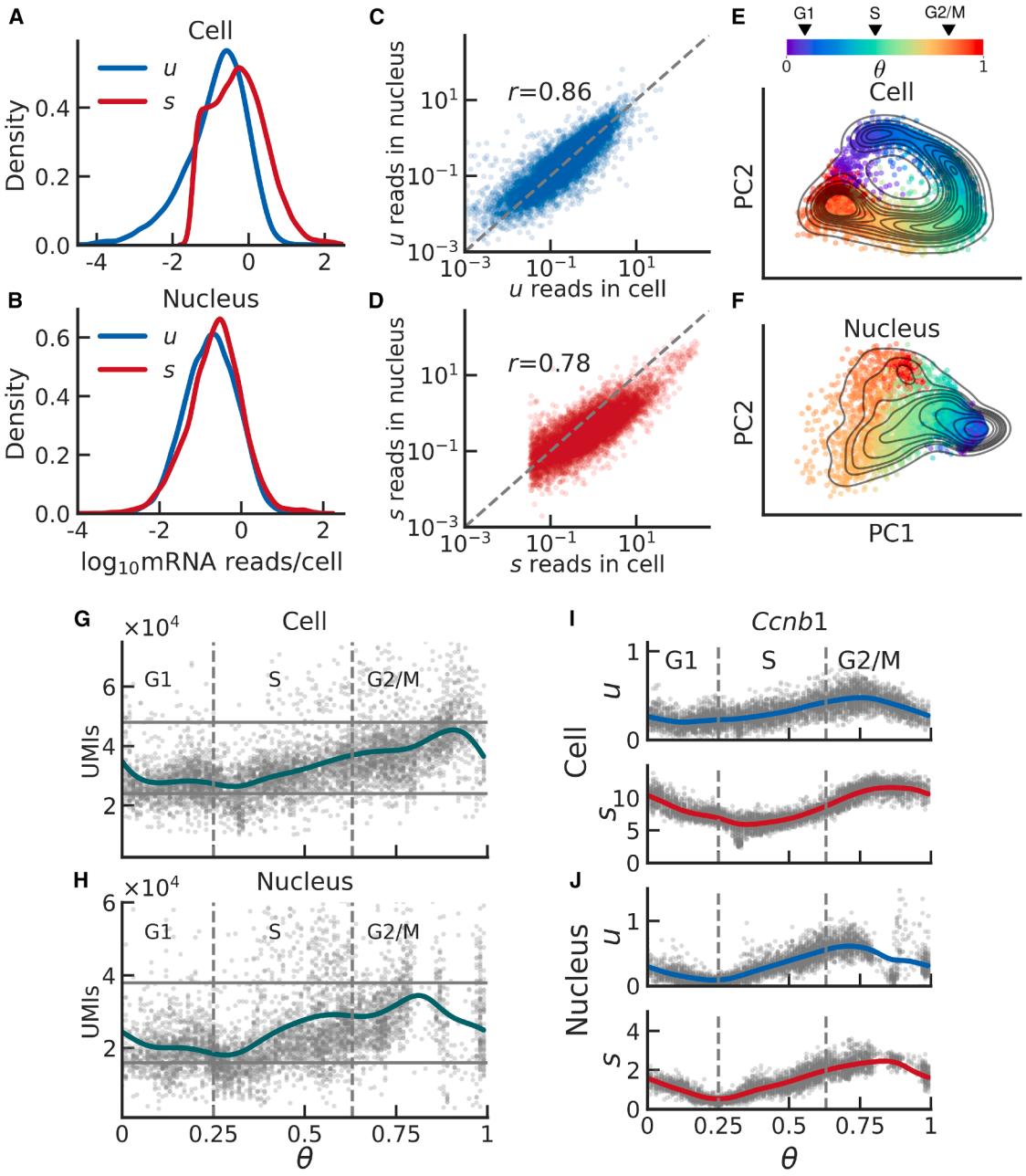

Figure 1. DeepCycle infers the cell cycle phase of both single cells and single nuclei

(A and B) Distribution of unspliced (blue) and spliced (red) reads per cell across all genes in the cell and the nucleus, respectively.

(C and D) Correlation between the reads in the cell versus those in the nucleus for the unspliced (blue) and spliced (red) molecules, respectively; every dot represents a gene.

(E and F) Visualization of the cycling dynamics based on the sequencing profiles of the cells and isolated nuclei, respectively; every dot represents a cell, and the color indicates the progression through the cell cycle—early G1 (in purple) through mitotic (in red).

(G and H) Unique molecular identifiers (UMIs), a proxy for the total mRNA content in the cell and the nucleus, respectively, against the cell cycle phase θ; there is a 2-fold change in the total mRNA content, both in the nucleus and in the cell, during the cell cycle.

(I and J) Expression dynamics of the unspliced and spliced reads for *Ccnb1* in the cell and the nucleus, respectively. The cell cycle phase transitions are represented with gray dotted lines and obtained using our previously described approach.[11] The gray dots get scarce as θ approaches 0 or 1; this is likely because the nuclear envelope breaks down during mitosis and the sequencing technique is unable to profile these nuclei.

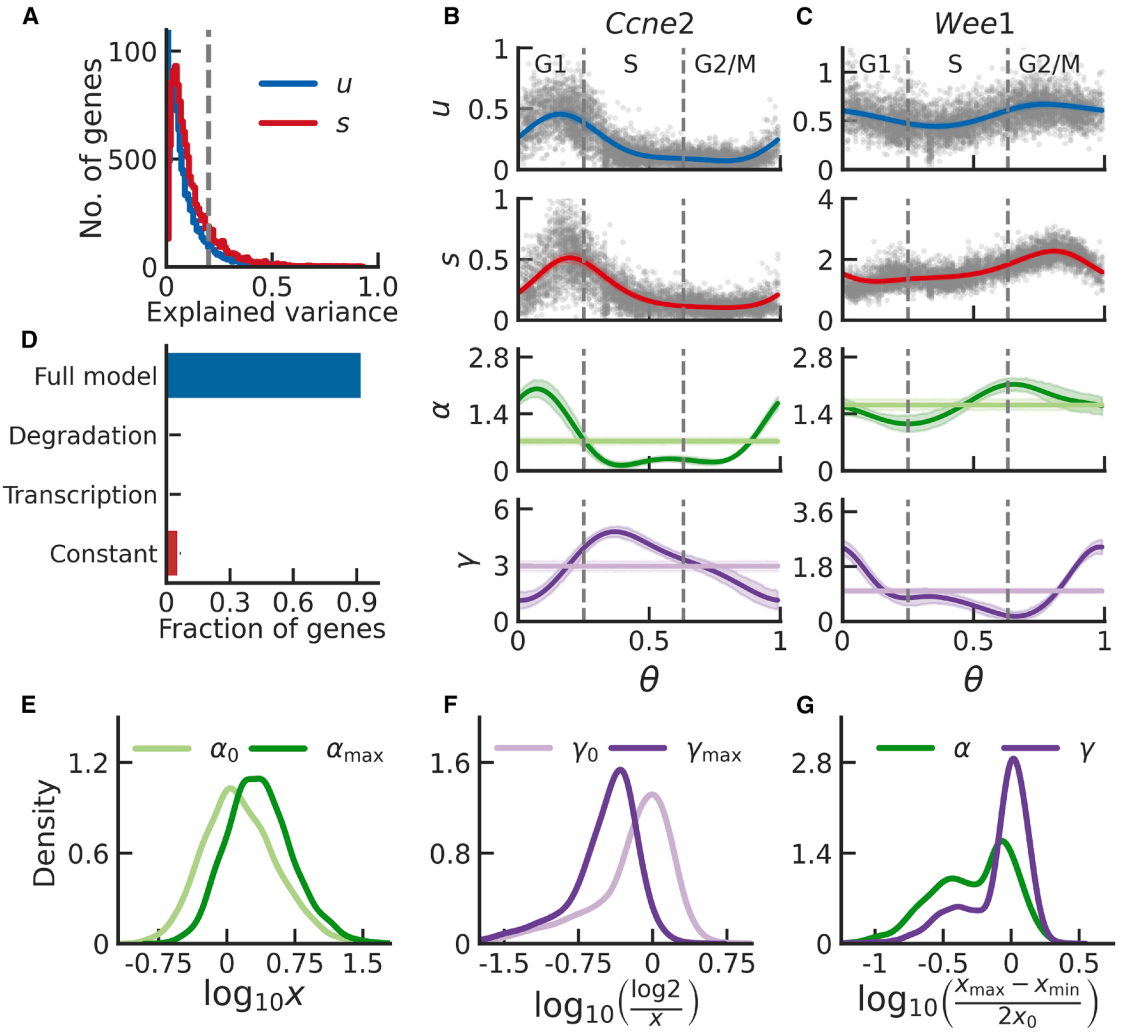

Figure 2. Genome-wide estimation of global transcription and degradation rates and characterization of transcriptional and post-transcriptional regulation

(A) Histogram of the explained variance for an oscillatory dynamics in unspliced (in blue) and spliced (in red) expression levels across all the genes; the dotted line is at $x = 0.2$, the threshold of explained variance for filtering genes.

(B and C) Top to bottom: number of unspliced reads (u), number of spliced reads (s), transcription rate (α), and degradation rate (γ) as a function of the cell cycle phase θ. Gray dots represent single cells, solid lines show model predictions, and shaded regions are 95% confidence intervals from bootstrapping.

(D) Barplot of fraction of genes selecting alternative models based on the Bayesian information criterion—full model (blue); model with cell-cycle-dependent degradation and constant splicing and transcription (purple); model with cell-cycle-dependent transcription and constant splicing and degradation (green); and model with constant transcription, splicing, and degradation (red). For the vast majority of the genes, the full model is preferred.

(E) Distribution of transcription rate, in arbitrary units, across filtered genes. α_0 denotes baseline transcription (light green), whereas α_{max} denotes maximum transcription rate (green).

(F) Distribution of degradation half-lives, in hours, across filtered genes. γ_0 denotes baseline degradation rate (light purple), whereas γ_{max} denotes maximum degradation rate.

(G) Fold change in amplitude of rates, $(x_{max} - x_{min})/2$, over the baseline rate for transcription (in green) and degradation (in purple). For most of the genes, the changes in degradation rates are more prominent than those in transcription rates compared to the corresponding baseline rates.

using a Fourier series expansion (details provided in the supplemental information). Finally, we used normalized unspliced and spliced reads, along with the cell cycle phase, as observable variables to fit the fundamental rates of RNA metabolism (details in the STAR Methods section).

Before proceeding with fitting the model to the sequencing data, we filtered genes that exhibit oscillatory dynamics in gene expression with respect to θ. Briefly, we calculated the explained variance, r^2, using periodic kernel smoothing of the unspliced and spliced expression levels of all genes. Figure 2A shows the distribution of explained variances for unspliced and spliced levels for all genes. We used a threshold of $r^2 > 0.2$ in unspliced or spliced gene expression, and 2,762 out of roughly 12,000 genes satisfied this cutoff (4,903 and 4,098

for snRNA-seq replicates 1 and 2, respectively; this number is higher than that for scRNA-seq, which could be explained by the superior capture efficiency of intronic reads in the case of the snRNA-seq when compared to scRNA-seq, which directly impacts the RNA-velocity framework). Genes that were excluded either did not show an oscillatory expression profile or the noise level was too high to detect a dynamic pattern (see Figure S3 and STAR Methods section). All downstream analyses were restricted to the filtered genes; however, for the sake of visualization, we provide model predictions for all genes on the FourierCycle webserver. Note that genes with lower explained variances also tend to have lower gene expression, with the exception of housekeeping genes, such as ribosomal proteins small and large subunits (Rps and Rpl, respectively), and intronless genes, such as mitochondrial genes.

Our biophysical model revealed the dynamics of the unspliced and spliced mRNA levels, leading to an estimation of the dynamics of the transcription and degradation rates (see the representative genes *Ccne1* and *Wee1*; Figures 2B and 2C). *Ccne2* encodes the G1/S-specific cyclin-E2 protein, essential for cell cycle control during the late G1/early S phase,[26,27] whereas *Wee1* acts as a negative regulator of entry into mitosis.[28,29] In agreement with these established functions, we observed a significant increase in the *Ccne2* transcription rate during the G1/S transition (Figure 2B). Additionally, we noted that the degradation rate remains relatively constant, suggesting that the mRNA level of *Ccne2* is primarily regulated at the transcriptional level. Also in agreement with the literature, *Wee1* showed a sharp increase in mRNA degradation during the M/G1 transition, while its transcription rate did not fluctuate much relative to the baseline (Figure 2C). This suggests that, in the case of *Wee1*, mRNA expression is mainly regulated post-transcriptionally. To test the robustness of FourierCycle and solidify our claims, we used our approach on publicly available scRNA-seq data on mESCs with culture conditions that were similar to ours.[30] Note that the data have fewer reads per cell than ours; however, we observe similar trends in gene expression and transcriptional regulation dynamics (see Figure S5).

To determine, across the genome, which genes are preferentially regulated at the transcriptional or post-transcriptional level, we constructed three alternative models: one where only transcription is cell-cycle dependent (splicing and degradation remaining constant), another where only degradation was cell-cycle dependent (transcription and splicing remaining constant), and a third where transcription, splicing, and degradation all remain constant during the cell cycle. We fitted these models to the sequencing data and used the Bayesian information criterion (BIC; details in STAR Methods section) to perform model selection for every gene that exhibited oscillatory dynamics. We observed that the behavior of 92.5% of the genes was captured by a full model with cell-cycle-dependent transcription as well as degradation; 5.6% of the genes preferred the model with no cell-cycle dependence (constant model); 1.1% of the genes agreed with the model where only transcription is cell-cycle dependent; and 0.7% of the genes preferred the model where only degradation was cell-cycle dependent (Figure 2D). Overall, we were able to fit our biophysical model of mRNA metabolism to thousands of genes and found oscillatory dynamics for transcription and degradation.

We investigated the genome-wide synthesis and degradation rates for all the genes satisfying the explained variance cutoff mentioned above. We observed that the baseline transcription rates and degradation rates in mESCs span a large dynamic range across genes—more than two orders of magnitude (Figures 2E and 2F). Since the model was fitted to relative quantifications of unspliced and spliced reads, the numerical values of transcription rates in Figure 2E do not reflect the absolute number of molecules synthesized per hour; however, fold changes with respect to the baseline provide information on the transcriptional resources dedicated to a particular gene during cell cycle progression. On the contrary, the degradation half-lives were expressed in units of hours, assuming a typical cell cycle duration of 14 h (Figure 2F).[11] We found that the mean of the baseline degradation half-lives was around 52 min, whereas the mean of the maximum degradation half-lives was 11 min. These values overall agree with previously reported estimates of mRNA degradation rates.[31,32]

We also calculated the difference in time between peak spliced and peak unspliced levels; the median time difference is around one-tenth of a cycle, which translates to 1.4 h (Figure S6). To gain insight into the fold changes in the rate parameters, we calculated the amplitude of the rates, i.e., (max − min)/2, and compared it to the baseline rates (Figure 2G). For most of the genes, the fold change in amplitude for mRNA degradation is higher than for transcription. Model selection using BIC suggests that regulation of mRNA metabolism requires both transcription and degradation to be cell-cycle dependent; however, for the majority of genes, the changes in mRNA degradation rates contribute more to regulating gene expression dynamics than the changes in transcription. Therefore, mRNA post-transcriptional regulation has a prominent role in shaping mRNA accumulation during the cell cycle.

Waves of transcriptional and post-transcriptional regulation during the cell cycle

After investigating the global trends in transcription and degradation rates, we examined the timing of peak rates of transcription and degradation during the cell cycle for the filtered genes. We observed distinct waves of mRNA synthesis during the cell cycle (Figure 3A), with 1,178 genes (46.5% of the 2,762 filtered) achieving peak transcription during the G1 phase, 554 genes (21.8%) during the S phase, and 804 genes (31.7%) during the G2/M phase. In terms of mRNA degradation, we found that 1,028 (40.5%) genes achieved peak degradation during the G1 phase, 909 (35.8%) genes during the S phase, and 599 (23.6%) genes during the G2/M phase (Figure 3B). Interestingly, we observed a prominent wave of maximum transcription in the early G1 phase (Figure 3A) and waves of degradation concentrated mainly during G1 and S phases (Figure 3B). Next, we normalized the predicted transcription and degradation rates across all cells and arranged genes based on the timing of their peak transcription (Figures 3C and 3D), observing the same wave patterns. However, each of these waves consists of a distinct set of genes. For example, during the G1, the mESCs upregulate genes involved in fundamental processes essential for

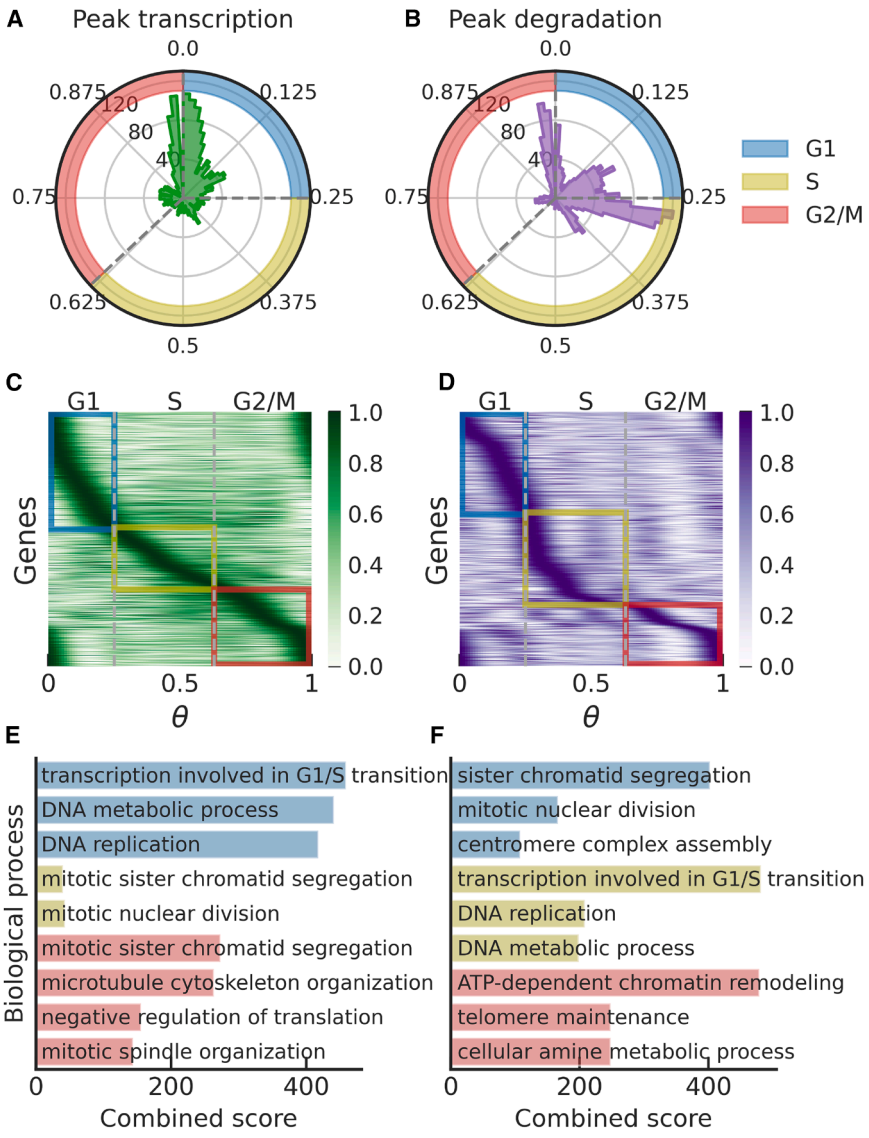

Figure 3. Waves of transcription and degradation and the biological processes involved during the cell cycle

(A and B) Polar histograms of the cell cycle phase at which a gene achieves the highest transcription rate and the highest degradation rate, respectively.

(C and D) Heatmaps of transcription and degradation, respectively, during the cell cycle. The rates are normalized using max-min normalization, and the genes are arranged based on the timing of the maximum rate. Genes that achieve their peak transcription and degradation rates during G1, S, and G2/M phases are highlighted in light blue, olive, and pink, respectively.

(E and F) Gene set enrichment analysis[33,34] for genes that achieve peak transcription and degradation, respectively; gene sets were compared against Gene Ontology (GO) biological processes (2018 released). The length of the bar represents the combined enrichement score for the process.

cell growth and proliferation (e.g., amine metabolism, DNA replication initiation, and cell cycle G1/S phase transition) (Figure 3E). On the other hand, the S phase involves peak transcription of genes involved in preparing cells for mitosis, and the G2/M phase is associated with the synthesis of genes involved in a variety of mitosis-related pathways (Figure 3E). The enrichment analysis of the degradation waves revealed many of the same processes; however, they tended to peak at different times, consistent with the need to remove transcripts of proteins that are no longer functionally needed (Figure 3F). As such, the degradation wave during the G1 phase consists of genes that are involved in mitotic regulation, as genes produced during the G2/M phase are degraded upon entering the G1 phase when they are no longer needed. Similarly, during the S phase, the mESCs degrade genes involved in processes such as DNA replication initiation and G1/S phase transition, which achieved peak transcription during the G1 phase. Overall, these results suggest that waves of transcription and mRNA degradations occur at well-defined points of the cell cycle. We speculate that they enable the cell to produce transcripts (ultimately proteins) needed at specific points of the cell cycle en masse and put a stop to their activity by waves of mRNA degradation.

Genome-wide estimates of mRNA nuclear export rates and waves of nuclear export

Nuclear mRNA export is another process that could affect mRNA metabolism. To measure mRNA export rates and their changes during the cell cycle, we constructed a biophysical model that attributes changes in abundance of mRNA in the nucleus to transcription, splicing, and nuclear export, denoted by η. This model makes an assumption that nuclear export exerts a much stronger influence over mRNA abundance in the nucleus than degradation, which may be a reasonable scenario given that nuclear export is a faster process than nuclear degradation.[35]

Figures S7A–S7D show the oscillatory dynamics in unspliced, spliced, transcription, and nuclear export rates for representative genes, *Ccne2* and *Wee1*. As seen in the case of transcription and degradation, nuclear retention half-lives span a large dynamic range, with a mean baseline half-life of 16 min and a mean maximum half-life of 8 min (Figures 4A and 4B). The distribution of fold change in amplitude over the baseline for nuclear export half-lives was between 0.001 and 78.1 (Figure 4B), indicating that for some genes, the change in export rate can play a significant role in the dynamics of mRNA accumulation during the cell cycle. We found that the majority of genes (94.2%) prefer the full model (transcription, splicing, and nuclear export)

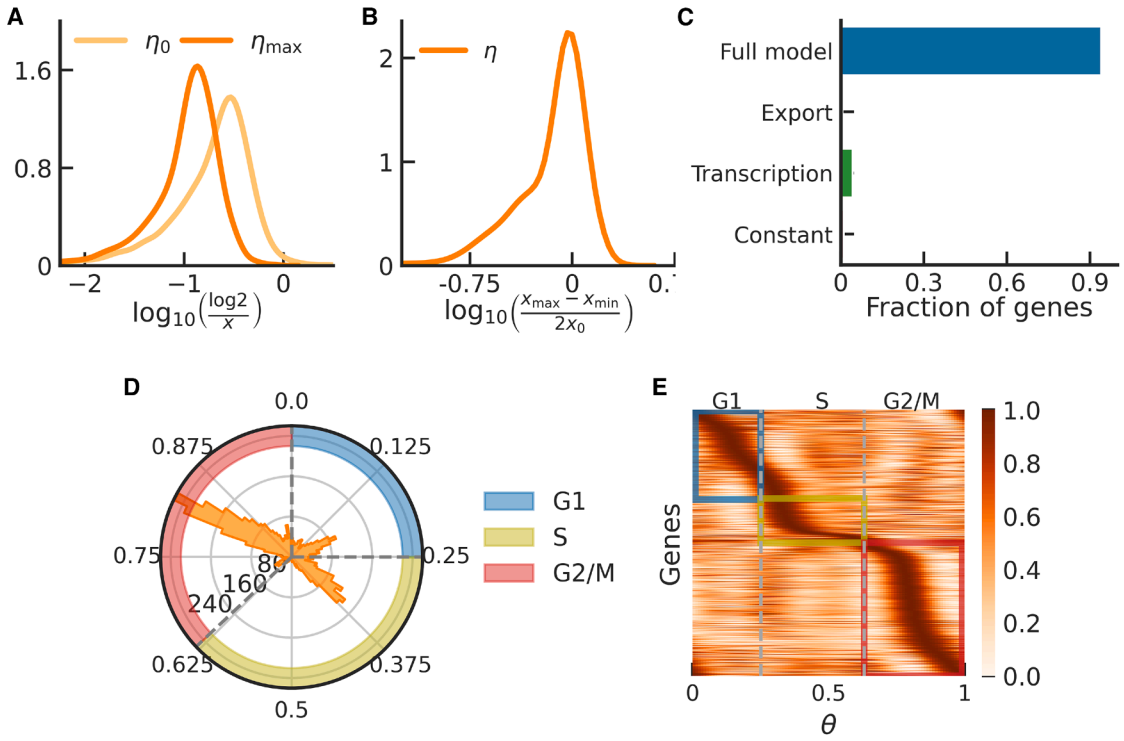

Figure 4. Genome-wide estimation of global export rates and characterization of waves of export during the cell cycle

(A) Distribution of export half-lives, per hour, for baseline export rate (light orange) and maximum export rate (orange); export rates span a large range, and the mean baseline export half-life is 16 min.

(B) Distribution of fold change in amplitude over baseline.

(C) Barplot of fraction of genes selecting alternative models based on BIC—full model (blue); model with cell-cycle-dependent export and constant splicing and transcription (purple); model with cell-cycle-dependent transcription and constant splicing and export (green); and model with constant transcription, splicing, and export (red). For the vast majority of the genes, the full model is preferred.

(D) Polar histogram of the cell cycle phase at which a gene achieves the highest export rate.

(E) Heatmaps of nuclear export during the cell cycle; the rates are normalized using max-min normalization, and the genes are arranged based on the timing of maximum export rate.

(Figure 4C), indicating that nuclear mRNA retention may be regulated during the cell cycle. For 4.3% of the genes, we found that only transcription was cell-cycle dependent, and only 1% of the genes preferred a model with constant rates. We also examined the timing of peak transcription and export rates. Strikingly, our method uncovers very prominent waves of nuclear export during the cell cycle (Figures 4D and S9). Of the 4,903 genes that satisfied the explained variance criterion, 1,591 (33.1%) genes achieved peak export during the G1 phase, 746 (15.5%) genes during the S phase, and 2,467 (51.4%) genes during the G2/M phase (Figures 4D and 4E). Note that the peak export during the G2/M phase is most likely a consequence of the breakdown of the nuclear envelope during mitosis, and with our approach, we can identify which mRNA transcripts are affected by this event. There is an abundance of recent literature on measuring mRNA export turnover rates using a variety of experimental techniques,[35–41] albeit not all of them report the dynamics in these rates. We compared the baseline degradation and export rates predicted by FourierCycle with values reported by the studies that are most relevant to ours and found that our predictions were in agreement with these values (see Figure S10). Taking these results together, we identified evidence that mRNA nuclear export was cell-cycle dependent.

Dynamics of chromatin accessibility during the cell cycle

The multiome profiling provides information about chromatin accessibility in addition to gene expression data for the same cells. This feature gave us the unique opportunity to investigate chromatin accessibility dynamics throughout the cell cycle by combining cell cycle phase information with chromatin accessibility readouts. First, we mapped the ATAC fragments to chromatin states in mESCs provided by ChromHMM.[42,43] To increase the sample size, we combined ATAC reads from the two replicates that were mapped to the same genomic regions. Note that as a consequence of DNA synthesis, we have twice as much genetic material in cells that have progressed through the S phase; to account for this, we normalized the ATAC reads by the total number of reads in the cell. Single-cell resolution accessibility is extremely sparse; thus, to improve statistical power, we divided the θs into 100 distinct bins and obtained the average reads for all the cells that belonged to a particular θ bin. This is a

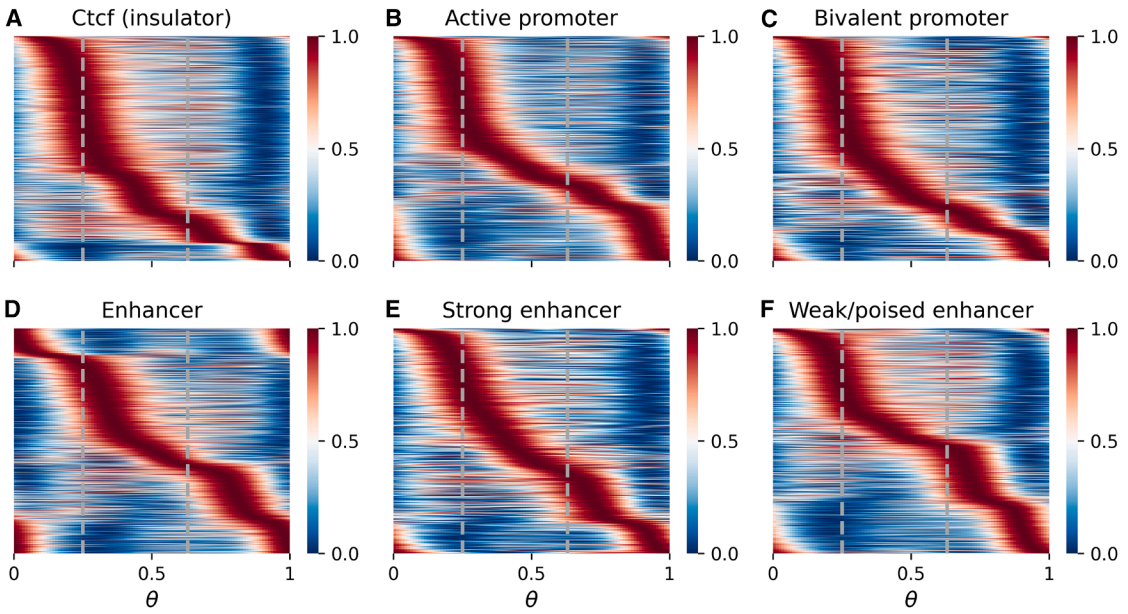

Figure 5. Chromatin accessibility of regulatory regions during the cell cycle

Chromatin accessibility was normalized by cell and then pseudo-bulked into 100 distinct values of θs. We then perfomed a moving average using a periodic Gaussian kernel and did a max-min normalization to have accessibility values between 0 and 1. Shown are the accessibility profiles of the (A) transcription factor CTCF. (B) active promoter, (C) bivalent promoter, (D) enhancer, (E) strong enhancer, and (F) weak/poised enhancer.

common approach and is often referred to as "pseudo-bulking." We then calculated the moving averages over the cell cycle phases for every region present in the chromatin states, and to aid with visualization, we performed max-min normalization. The heatmaps in Figure 5 show the accessibility dynamics of select regulatory regions in mESCs, namely, CTCF binding sites, active promoters, bivalent promoters, enhancers, strong enhancers, and weak/poised enhancers. For all of these regulatory regions, we found that there was a specific order in which the regulatory regions became accessible during the cell cycle. We also see a global decline in accessibility across all regions, likely due to chromatin compactification during mitosis. We found that most of the regulatory regions comprising CTCF binding sites, active promoters, and bivalent promoters have maximal accessibility during the G1 phase. Interestingly, the majority of enhancers are accessible during the S phase, and some are available during the G2/M phase. Also, a significant fraction of weak enhancers are accessible during the G2/M phase.[44,45] In conclusion, our analysis reveals that chromatin accessibility follows a defined temporal pattern during the cell cycle, highlighting the interplay between chromatin structure and cell cycle progression.

Chromatin accessibility dynamics within TF footprints reveal key cell cycle regulators

ATAC-seq data have been instrumental in characterizing TF footprints within accessible chromatin regions.[46] Our single-nuclei multiome experiments, together with computational cell cycle sorting, allowed us to investigate the dynamic changes of TF footprints throughout the cell cycle. To that end, we first used a set of known position weight matrices (PWMs) of 678 TFs to identify putative binding sites on the DNA within ATAC peaks found by CellRanger.[47] We then calculated TF footprints by combining all of the observed Tn5 cuts at a given distance with respect to the predicted binding site (see STAR Methods). This strategy produced average footprints for individual TFs and revealed distinct profiles, as illustrated for two representative factors, Tfcp2l1 and Pml (Figure 6A). By repeating the same analysis considering nuclei in a specific cell cycle phase bin, we calculated how the footprints fluctuate with respect to the average throughout the cell cycle (Figure 6B). Interestingly, we observed an increase in chromatin accessibility around Tfcp2l1 binding sites during the G1-S transition, reaching a minimum during the G2-M transition (Figures 6C and 6D). In contrast, the chromatin accessibility around binding sites of Pml exhibited a pronounced maximum during the G2-M transition (Figures 6C and 6D). These changes in the TF footprints suggest potential variations in the binding activity of these TFs across different cell cycle phases. The changes in acessibility of TF footprints duirng the cell cycle (Figure 6E) revealed several known cell cycle regulators—such as Chd1, E2f1, Nfya, and Nrf1—among the top candidates, supporting our approach (see Table S1). Overall, our method identifies phase-specific TF binding dynamics, offering insights into transcriptional regulation during the cell cycle. In summary, our method unveiled distinct cell-cycle-dependent changes in TF footprints of chromatin accessibility, generating predictions of the specific phases when TFs are likely to actively interact with DNA and potentially regulate transcription during the cell cycle.

DISCUSSION

The RNA-velocity framework uses single-cell sequencing data (static information) to infer how gene expression changes

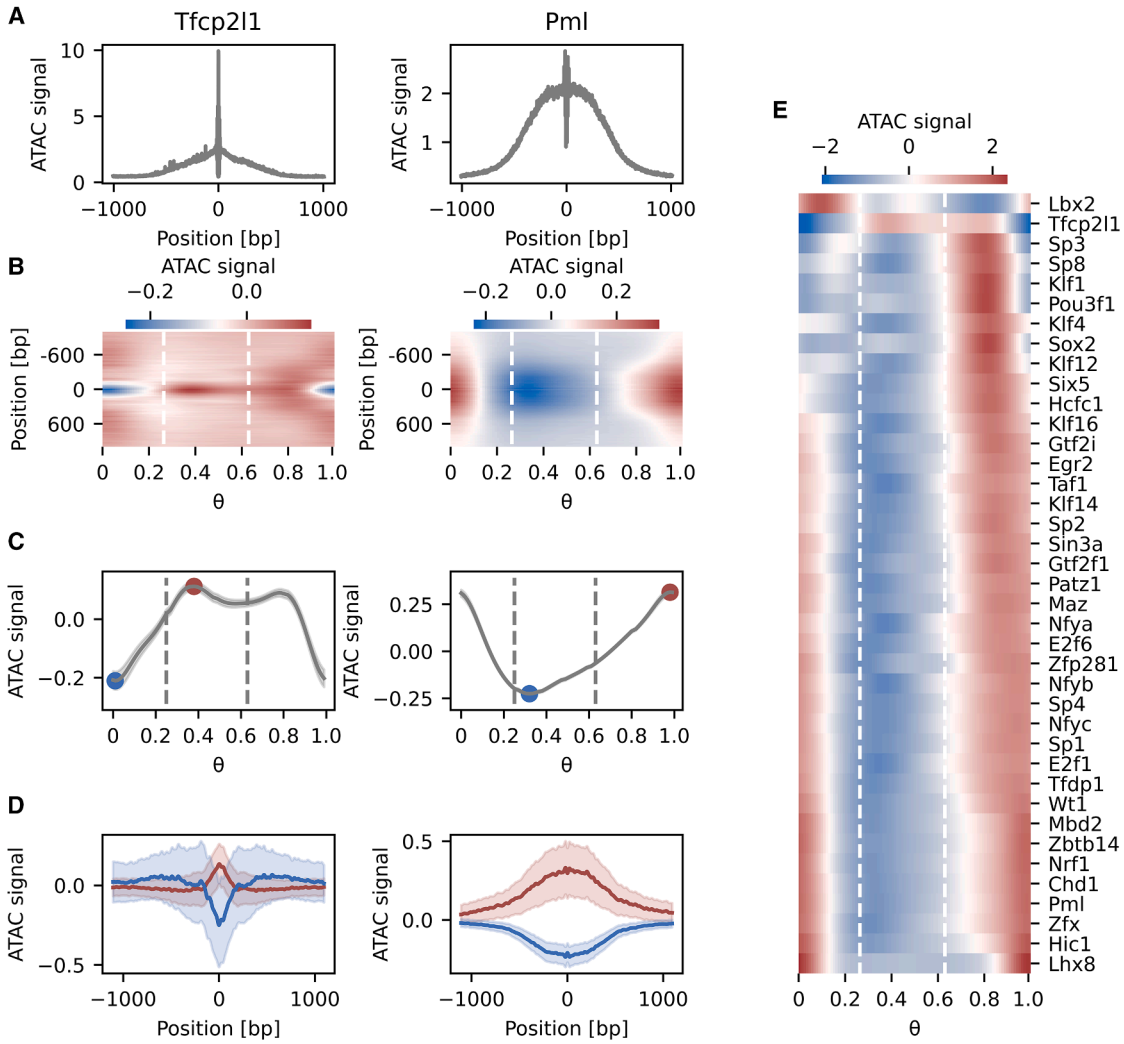

Figure 6. TF footprint dynamics during the cell cycle uncover key cell cycle regulators

(A) Average ATAC-seq footprints of TFcp2l1 and Pml showing the normalized number of Tn5 cuts centered relative to predicted binding sites within ATAC peaks.

(B) Cell cycle dynamics of the Tfcp2l1 and Pml footprints as a function of the cell cycle phase θ relative to the average footprint depicted in (A). White dashed lines delimit cell cycle phases in the following order: G1, S, and G2/M.

(C) Changes in chromatin accessibility during the cell cycle averaged within a 100 bp window centered at the TF binding site. Maximum and minimum accessibilities are indicated in red and blue, respectively. Gray dashed lines delimit cell cycle phases in the following order: G1, S, and G2/M.

(D) Relative TF footprint at the maximum (red) and minimum (blue) of accessibility as indicated in (C). Shaded areas represent standard deviations.

(E) Changes in averaged chromatin accessibility around binding sites of the top 40 TFs for which the change is most significant. White dashed lines delimit cell cycle phases in the following order: G1, S, and G2/M.

over time and characterize gene expression dynamics in various biological contexts.[14,15] DeepCycle uses the RNA-velocity framework to infer the cell cycle phase based on the unspliced and spliced levels of pre-selected cycling genes, and it reveals the oscillatory dynamics of gene expression at a very high temporal resolution.[11] In this work, using FourierCycle, we examined the relationship between the cell cycle and the different processes involved in mRNA metabolism (transcription, splicing, mRNA degradation, and mRNA nuclear export) and discovered oscillatory dynamics of mRNA metabolism and waves of transcriptional and post-transcriptional regulation during the cell cycle.

To dissect different processes that affect the relationship between the cell cycle and mRNA metabolism, we constructed biophysical models that make genome-wide predictions for the cell-cycle dependence of transcription, nuclear export, and degradation rates in mESCs. These models also give insights about the timing of the up- or downregulation of cellular biological processes during the cell cycle. Our predictions for the baseline rates, i.e., the cell-cycle-independent rates, were in agreement with the available literature,[31,32] validating our approach. It is relevant to point out that although the measurements for the rate parameters in the literature are derived from a variety of experiments, our biophysical models allow us to make

predictions for all of these rate parameters based on a single experiment. Comparing the BIC score for alternate models, we found that for most of the oscillating genes, the full model that incorporates cell-cycle-dependent transcription, splicing, and mRNA nuclear export is preferred. Importantly, we found that cell-cycle-dependent changes in post-transcriptional regulation control the gene expression dynamics in proliferating mESCs to a greater extent than cell-cycle-dependent transcription.

Our approach allowed us to examine the timing of peak rates, leading to the discovery of prominent waves of transcription, export, and degradation during the cell cycle. We found that nearly half of the oscillating genes achieved peak transcription during the early G1 phase. This phenomenon has been previously shown in synchronized cell populations.[9,48,49] To the best of our knowledge, this is the first time it is reported in unperturbed and unsynchronized mESCs. The peak transcription of the remainder of the genes is more evenly distributed throughout the cell cycle. The dynamics of nuclear export remains extremely poorly characterized, primarily due to a lack of reliable transcriptomic measurements for the nucleus. Here, we debut a genome-wide estimation of nuclear export rates and find that nearly 50% of the genes achieve maximal export in the G2/M phase. Therefore, the disconnect between peak transcription rates and peak export rates hints at preferential nuclear retention of mRNA transcripts. We also observed that mRNA degradation waves are distinct from waves in transcription and export, with one wave occurring at around 25 min of reentry into G1, another in late G1, and the third in early S phase. These results are in line with recent work by Krenning et al. that reported two distinct waves of mRNA degradation in RPE1 cells—an immediate wave within 20 min after metaphase and a delayed wave roughly 80 min after metaphase.[50] Taken together, the results of our analysis reveal the existence of distinct waves of transcription, mRNA nuclear export, and mRNA degradation that occur at different points in the cell cycle to allow the cell to achieve tight temporal control over this complex process. Furthermore, to the best of our knowledge, this is the first time that genome-wide transcriptional and post-transcriptional waves have been reported during the cell cycle using scRNA-seq profiles. The advent of multiome single-cell profiling has made it possible to simultaneously profile gene expression as well as chromatin accessibility at single-cell resolution. This provided us with a unique opportunity to investigate accessibility dynamics during the cell cycle progression. One of the surprising findings that emerged from this work was the observation that genome-wide chromatin accessibility was the highest during the S/G2 transition, although one would expect that it would be highest during the S phase, when the DNA is being duplicated. On the other hand, normalized accessibility does show a peak in accessibility during the G1/S transition that stays relatively high during the S phase and undergoes a global dip during mitosis due to chromatin condensation. We were also able to probe gene-wise chromatin accessibilities and compare them with the gene expression readouts from snRNA-seq data, as exemplified by Ccnb2, Nusap1, and Kif2c. We found hints of differential mechanisms involved in regulating the steps between chromatin accessibility and active transcription of associated genes.

Importantly, this paper describes an important extension of DeepCycle, as we validate that it can handle not only scRNA-seq data but snRNA-seq data as well. Our analysis of snRNA-seq enabled us to observe that the number of mRNA molecules in the nucleus increases during the cell cycle, which builds on previous observations that this also occurs in the cytoplasm.[11] This suggests that the local mRNA concentration stays constant during the cell cycle in both the cytoplasm and the nucleus. We also found extremely strong correlations in reads from scRNA-seq and snRNA-seq, even though these are two completely different experimental protocols, giving us confidence in the quality of the measurements.

In conclusion, FourierCycle combines single-cell multiome sequencing and biophysical modeling to build a high-resolution map of the entire cell cycle transcriptome. This represents a powerful approach for genome-wide, single-cell studies of transcriptional dynamics throughout the cell cycle. Thus, FourierCycle and the underlying data we report here will serve as valuable resources for the community and enable dissection of regulatory mechanisms involved in oscillatory dynamics of mRNA metabolism during the cell cycle. Additionally, the scope of FourierCycle is not limited to *in vitro* models, as it could be easily extended to other systems, such as organoids or patient samples, and used to better understand cell-cycle-related mechanisms in development and disease biology.

Limitations of the study

Single-cell sequencing technologies are inherently noisy, more so in the case of multiome sequencing, where the genetic material from a single nucleus is shared between two experiments. We found extremely good concurrence in analysis between the two replicates using snRNA-seq, which indicates high quality of our data. Recent work by Gorin et al. highlighted the shortcomings of the RNA-velocity framework concerning both the underlying assumption of the biophysical model and the preprocessing of the data.[51] Our approach mitigates some of these limitations; specifically, we do not assume constant production and degradation rates, our system does not have multiple cell identities, and most of the biological variability arises from the cell cycle. DeepCycle is most effective for cells that are largely proliferative, and we would not recommend its use in quiescent, senescent, or heterogeneous cell populations. Our future work will focus on addressing some of these challenges and expanding the utility of DeepCycle further.

The noise model that we use in this work, log-normal, may not be the most appropriate for single-cell sequencing data. One could improve this either by using a more accurate noise model to capture the intrinsic and technical fluctuations in the data or by adapting the approaches in Volteras et al.,[40] Tang et al.,[41] and Gorin et al.[51]

In this study, we focus on a phenomenological description of cell-cycle-dependent transcription, export, and degradation rates without attempting to uncover the underlying molecular mechanisms. Dynamic TF activity and chromatin remodeling could underlie the observed transcriptional dynamics, while cell-cycle-regulated RNA-binding proteins may contribute to changes in export and degradation rates. Additionally, other biological processes, such as translation, could feed back into

mRNA stability and influence the inferred rate dynamics. Thus, our work opens new avenues for research.

RESOURCE AVAILABILITY

Lead contact

Requests for further information and resources should be directed to and will be fulfilled by the lead contact, Nacho Molina (molinan@igbmc.fr).

Materials availability

This study did not generate new unique reagents or cell lines.

Data and code availability

- Raw and processed data of multiome profiling, snRNA-seq, and snATAC-seq of mESCs cultured in 2i and LIF in serum-supplemented conditions have been deposited on GEO with accession code GEO: GSE300730[52] (https://www.ncbi.nlm.nih.gov/geo/query/acc.cgi?acc=GSE300730).
- The code base for FourierCycle[17] has been deposited on GitHub (https://github.com/MolinaLab-IGBMC/FourierCycle).
- Results from the FourierCycle analysis have been deposited on Zenodo[53]: https://doi.org/10.5281/zenodo.10462840. The results can also be explored through an interactive online webserver: https://molina.igbmc.science/FourierCycle-Home.html.

ACKNOWLEDGMENTS

We are grateful to Manuel Mendoza, Bertrand Séraphin, Georg Stoecklin, and Jingkui Wang for their thorough review and constructive criticism, which greatly improved the overall quality of this manuscript. This work of the Interdisciplinary Thematic Institute IMCBio+, as part of the ITI 2021–2028 program of the University of Strasbourg, CNRS, and INSERM, was supported by IdEx Unistra (ANR-10-IDEX-0002) and by the SFRI-STRAT'US project (ANR-20-SFRI-0012) and EUR IMCBio (ANR-17-EURE-0023) under the framework of the France 2030 Program. This work was also supported by the fellowship USIAS-2021-045 from the University of Strasbourg Institute for Advanced Study (USIAS). Library preparation and sequencing were performed by the GenomEast platform, a member of the France Génomique consortium (ANR-10-INBS-0009). Icons used in the graphical abstract made by dDara (cell), Dimitry Mirolibov (DNA), Mayor Icons (anaphase), and Freeplk (cytokinesis) are from www.flaticon.com.

AUTHOR CONTRIBUTIONS

Conceptualization, N.M. and M.K.N.; methodology, N.M. and M.K.N.; formal analysis, M.K.N. and A.R.; investigation, D.S.-A. and M.C.; data curation, O. T. and T.Y.; software, M.K.N.; visualization, M.K.N. and O.T.; writing – original draft, M.K.N. and N.M.; writing – review & editing, D.S.-A. and O.T.; funding acquisition, N.M.; project administration, N.M.; supervision, N.M.

DECLARATION OF INTERESTS

The authors declare no competing interests.

DECLARATION OF GENERATIVE AI AND AI-ASSISTED TECHNOLOGIES IN THE WRITING PROCESS

During the preparation of this work, the authors used ChatGPT 4o to proofread the manuscript. After using this tool or service, the authors reviewed and edited the content as needed and take full responsibility for the content of the publication.

STAR★METHODS

Detailed methods are provided in the online version of this paper and include the following:

SUPPLEMENTAL INFORMATION

Supplemental information can be found online at https://doi.org/10.1016/j.celrep.2025.116089.

Received: November 19, 2024
Revised: May 27, 2025
Accepted: July 11, 2025
Published: August 2, 2025

REFERENCES

1. Alberts, B., Johnson, A., Lewis, J., Morgan, D., Raff, M., Roberts, K., and Peter, W. (2002). Molecular Biology of the Cell, 6th edition (Garland Science).
2. Nurse, P. (2000). A long twentieth century of the cell cycle and beyond. Cell *100*, 71–78.
3. Hartwell, L.H., Culotti, J., Pringle, J.R., and Reid, B.J. (1974). Genetic control of the cell division cycle in yeast. Science *183*, 46–51.
4. Nurse, P. (1975). Genetic control of cell size at cell division in yeast. Nature *256*, 547–551. https://doi.org/10.1038/256547a0.
5. Pardee, A.B. (1974). A restriction point for control of normal animal cell proliferation. Proc. Natl. Acad. Sci. USA *71*, 1286–1290. https://doi.org/10.1073/pnas.71.4.1286.
6. Hartwell, L.H. (1978). Cell division from a genetic perspective. J. Cell Biol. *77*, 627–637. https://doi.org/10.1083/jcb.77.3.627.
7. Nurse, P., and Bissett, Y. (1981). Gene required in g1 for commitment to cell cycle and in g2 for control of mitosis in fission yeast. Nature *292*, 558–560. https://doi.org/10.1038/292558a0.
8. Rosenthal, E.T., Hunt, T., and Ruderman, J.V. (1980). Selective translation of mrna controls the pattern of protein synthesis during early development of the surf clam, *Spisula solidissima*. Cell *20*, 487–494. https://doi.org/10.1016/0092-8674(80)90635-2.
9. Palozola, K.C., Donahue, G., Liu, H., Grant, G.R., Becker, J.S., Cote, A., Yu, H., Raj, A., and Zaret, K.S. (2017). Mitotic transcription and waves of gene reactivation during mitotic exit. Science *358*, 119–122. https://doi.org/10.1126/science.aal4671.
10. Schwabe, D., Formichetti, S., Junker, J.P., Falcke, M., and Rajewsky, N. (2020). The transcriptome dynamics of single cells during the cell cycle. Mol. Syst. Biol. *16*, e9946. https://doi.org/10.15252/msb.20209946.
11. Riba, A., Oravecz, A., Durik, M., Jiménez, S., Alunni, V., Cerciat, M., Jung, M., Keime, C., Keyes, W.M., and Molina, N. (2022). Cell cycle gene regulation dynamics revealed by rna velocity and deep-learning. Nat. Commun. *13*, 2865. https://doi.org/10.1038/s41467-022-30545-8.
12. Zeisel, A., Köstler, W.J., Molotski, N., Tsai, J.M., Krauthgamer, R., Jacob-Hirsch, J., Rechavi, G., Soen, Y., Jung, S., Yarden, Y., and Domany, E. (2011). Coupled pre-mrna and mrna dynamics unveil operational strategies underlying transcriptional responses to stimuli. Mol. Syst. Biol. *7*, 529. https://doi.org/10.1038/msb.2011.62.

13. Gaidatzis, D., Burger, L., Florescu, M., and Stadler, M.B. (2016). Erratum: Analysis of intronic and exonic reads in rna-seq data characterizes transcriptional and post-transcriptional regulation. Nat. Biotechnol. *34*, 210. https://doi.org/10.1038/nbt0216-210a.

14. La Manno, G., Soldatov, R., Zeisel, A., Braun, E., Hochgerner, H., Petukhov, V., Lidschreiber, K., Kastriti, M.E., Lönnerberg, P., Furlan, A., et al. (2018). Rna velocity of single cells. Nature *560*, 494–498. https://doi.org/10.1038/s41586-018-0414-6.

15. Bergen, V., Lange, M., Peidli, S., Wolf, F.A., and Theis, F.J. (2020). Generalizing rna velocity to transient cell states through dynamical modeling. Nat. Biotechnol. *38*, 1408–1414. https://doi.org/10.1038/s41587-020-0591-3.

16. Liang, S., Wang, F., Han, J., and Chen, K. (2020). Latent periodic process inference from single-cell rna-seq data. Nat. Commun. *11*, 1441. https://doi.org/10.1038/s41467-020-15295-9.

17. Nariya, M., Santiago-Algarra, D., Tassy, O., Cerciat, M., Ye, T., Riba, A., and Molina, N. (2025). Fouriercycle: Cell cycle dependence of mrna metabolism using fourier series approximation. https://github.com/MolinaLab-IGBMC/FourierCycle accessed: 2025-06-26.

18. Navarro, P. (2018). 2i, or not 2i: The soliloquy of nanog-negative mouse embryonic stem cells. Stem Cell Rep. *11*, 1–3. https://doi.org/10.1016/j.stemcr.2018.06.017.

19. Hastreiter, S., Skylaki, S., Loeffler, D., Reimann, A., Hilsenbeck, O., Hoppe, P.S., Coutu, D.L., Kokkaliaris, K.D., Schwarzfischer, M., Anastassiadis, K., et al. (2018). Inductive and selective effects of gsk3 and mek inhibition on nanog heterogeneity in embryonic stem cells. Stem Cell Rep. *11*, 58–69. https://doi.org/10.1016/j.stemcr.2018.04.019.

20. Conklin, K. (2022). 10x genomics single-nucleus multiome (rna + atac) assay for profiling adult human tissues. . doi: https://doi.org/10.17504/protocols.io.5qpvoby69l4o/v2.

21. Islam, S., Zeisel, A., Joost, S., La Manno, G., Zajac, P., Kasper, M., Lönnerberg, P., and Linnarsson, S. (2014). Quantitative single-cell rna-seq with unique molecular identifiers. Nat. Methods *11*, 163–166. https://doi.org/10.1038/nmeth.2772.

22. Kou, R., Lam, H., Duan, H., Ye, L., Jongkam, N., Chen, W., Zhang, S., and Li, S. (2016). Benefits and challenges with applying unique molecular identifiers in next generation sequencing to detect low frequency mutations. PLoS One *11*, e0146638. https://doi.org/10.1371/journal.pone.0146638.

23. Padovan-Merhar, O., Nair, G.P., Biaesch, A.G., Mayer, A., Scarfone, S., Foley, S.W., Wu, A.R., Churchman, L.S., Singh, A., and Raj, A. (2015). Single mammalian cells compensate for differences in cellular volume and dna copy number through independent global transcriptional mechanisms. Mol. Cell *58*, 339–352. https://doi.org/10.1016/j.molcel.2015.03.005.

24. Brown, N.R., Lowe, E.D., Petri, E., Skamnaki, V., Antrobus, R., and Johnson, L.N. (2007). Cyclin b and cyclin a confer different substrate recognition properties on cdk2. Cell Cycle *6*, 1350–1359. https://doi.org/10.4161/cc.6.11.4278.

25. Petri, E.T., Errico, A., Escobedo, L., Hunt, T., and Basavappa, R. (2007). The crystal structure of human cyclin b. Cell Cycle *6*, 1342–1349. https://doi.org/10.4161/cc.6.11.4297.

26. Lew, D.J., Dulić, V., and Reed, S.I. (1991). Isolation of three novel human cyclins by rescue of g1 cyclin (cln) function in yeast. Cell *66*, 1197–1206. https://doi.org/10.1016/0092-8674(91)90042-w.

27. Ohtsubo, M., Theodoras, A.M., Schumacher, J., Roberts, J.M., and Pagano, M. (1995). Human cyclin e, a nuclear protein essential for the g1-to-s phase transition. Mol. Cell Biol. *15*, 2612–2624. https://doi.org/10.1128/mcb.15.5.2612.

28. Watanabe, N., Broome, M., and Hunter, T. (1995). Regulation of the human wee1hu cdk tyrosine 15-kinase during the cell cycle. EMBO J. *14*, 1878–1891. https://doi.org/10.1002/j.1460-2075.1995.tb07180.x.

29. Elbaek, C.R., Petrosius, V., and Sørensen, C.S. (2020). Wee1 kinase limits cdk activities to safeguard dna replication and mitotic entry. Mutat. Res. Fundam. Mol. Mech. Mutagen. *819*, 111694. https://doi.org/10.1016/j.mrfmmm.2020.111694.

30. Hu, X., van Sluijs, B., García-Blay, Ó., Stepanov, Y., Rietrae, K., Huck, W.T.S., and Hansen, M.M.K. (2024). ARTseq-FISH reveals position-dependent differences in gene expression of micropatterned mESCs. Nat. Commun. *15*, 3918.

31. Yang, E., van Nimwegen, E., Zavolan, M., Rajewsky, N., Schroeder, M., Magnasco, M., and Darnell, J.E. (2003). Decay rates of human mrnas: correlation with functional characteristics and sequence attributes. Genome Res. *13*, 1863–1872. https://doi.org/10.1101/gr.1272403.

32. Sharova, L.V., Sharov, A.A., Nedorezov, T., Piao, Y., Shaik, N., and Ko, M.S.H. (2009). Database for mrna half-life of 19, 977 genes obtained by dna microarray analysis of pluripotent and differentiating mouse embryonic stem cells. DNA Res. *16*, 45–58. https://doi.org/10.1093/dnares/dsn030.

33. Chen, E.Y., Tan, C.M., Kou, Y., Duan, Q., Wang, Z., Meirelles, G.V., Clark, N.R., and Ma'ayan, A. (2013). Enrichr: interactive and collaborative html5 gene list enrichment analysis tool. BMC Bioinf. *14*, 128. https://doi.org/10.1186/1471-2105-14-128.

34. Fang, Z., Liu, X., and Peltz, G. (2023). Gseapy: a comprehensive package for performing gene set enrichment analysis in python. Bioinformatics *39*, btac757. https://doi.org/10.1093/bioinformatics/btac757.

35. Ietswaart, R., Smalec, B.M., Xu, A., Choquet, K., McShane, E., Jowhar, Z.M., Guegler, C.K., Baxter-Koenigs, A.R., West, E.R., Fu, B.X.H., et al. (2024). Genome-wide quantification of rna flow across subcellular compartments reveals determinants of the mammalian transcript life cycle. Mol. Cell *84*, 2765–2784.e16. https://doi.org/10.1016/j.molcel.2024.06.008.

36. Steinbrecht, D., Minia, I., Milek, M., Meisig, J., Blüthgen, N., and Landthaler, M. (2024). Subcellular mrna kinetic modeling reveals nuclear retention as rate-limiting. Mol. Syst. Biol. *20*, 1346–1371. https://doi.org/10.1038/s44320-024-00073-2.

37. Lefaudeux, D., Sen, S., Jiang, K., Hoffmann, A., Miller, N., Cheng, Z., Chen, E.Y.H., Roy, S., Spreafico, R., et al.; UCLA Ribonomics Group (2022). Kinetics of mrna nuclear export regulate innate immune response gene expression. Nat. Commun. *13*, 7197. https://doi.org/10.1038/s41467-022-34635-5.

38. Battich, N., Beumer, J., de Barbanson, B., Krenning, L., Baron, C.S., Tanenbaum, M.E., Clevers, H., and van Oudenaarden, A. (2020). Sequencing metabolically labeled transcripts in single cells reveals mrna turnover strategies. Science *367*, 1151–1156. https://doi.org/10.1126/science.aax3072.

39. Liu, H., Arsiè, R., Schwabe, D., Schilling, M., Minia, I., Alles, J., Boltengagen, A., Kocks, C., Falcke, M., Friedman, N., et al. (2023). slam-drop-seq reveals mrna kinetic rates throughout the cell cycle. Mol. Syst. Biol. *19*, e11427. https://doi.org/10.15252/msb.202211427.

40. Volteras, D., Shahrezaei, V., and Thomas, P. (2024). Global transcription regulation revealed from dynamical correlations in time-resolved single-cell rna sequencing. Cell Syst. *15*, 694–708.e12. https://doi.org/10.1016/j.cels.2024.07.002.

41. Tang, W., Jørgensen, A.C.S., Marguerat, S., Thomas, P., and Shahrezaei, V. (2023). Modelling capture efficiency of single-cell rna-sequencing data improves inference of transcriptome-wide burst kinetics. Bioinformatics *39*, btad395. https://doi.org/10.1093/bioinformatics/btad395.

42. Ernst, J., and Kellis, M. (2012). Chromhmm: automating chromatin-state discovery and characterization. Nat. Methods *9*, 215–216. https://doi.org/10.1038/nmeth.1906.

43. Pintacuda, G., Wei, G., Roustan, C., Kirmizitas, B.A., Solcan, N., Cerase, A., Castello, A., Mohammed, S., Moindrot, B., Nesterova, T.B., and Brockdorff, N. (2017). hnrnpk recruits pcgf3/5-prc1 to the xist rna b-repeat to establish polycomb-mediated chromosomal silencing. Mol. Cell *68*, 955–969.e10. https://doi.org/10.1016/j.molcel.2017.11.013.

44. Friman, E.T., Deluz, C., Meireles-Filho, A.C., Govindan, S., Gardeux, V., Deplancke, B., and Suter, D.M. (2019). Dynamic regulation of chromatin

accessibility by pluripotency transcription factors across the cell cycle. eLife *8*, e50087. https://doi.org/10.7554/eLife.50087.

45. Lou, J., Rezvani, Y., Arriojas, A., Wu, Y., Shankar, N., Degras, D., Keroack, C.D., Duraisingh, M.T., Zarringhalam, K., and Gubbels, M.J. (2024). Single cell expression and chromatin accessibility of the toxoplasma gondii lytic cycle identifies ap2xii-8 as an essential ribosome regulon driver. Nat. Commun. *15*, 7419. https://doi.org/10.1038/s41467-024-51011-7.
46. Minnoye, L., Marinov, G.K., Krausgruber, T., Pan, L., Marand, A.P., Secchia, S., Greenleaf, W.J., Furlong, E.E.M., Zhao, K., Schmitz, R.J., et al. (2021). Chromatin accessibility profiling methods. Nat. Rev. Methods Primers *1*, 10. https://doi.org/10.1038/s43586-020-00008-9.
47. Satpathy, A.T., Granja, J.M., Yost, K.E., Qi, Y., Meschi, F., McDermott, G.P., Olsen, B.N., Mumbach, M.R., Pierce, S.E., Corces, M.R., et al. (2019). Massively parallel single-cell chromatin landscapes of human immune cell development and intratumoral t cell exhaustion. Nat. Biotechnol. *37*, 925–936. https://doi.org/10.1038/s41587-019-0206-z.
48. Hsiung, C.C.S., Bartman, C.R., Huang, P., Ginart, P., Stonestrom, A.J., Keller, C.A., Face, C., Jahn, K.S., Evans, P., Sankaranarayanan, L., et al. (2016). A hyperactive transcriptional state marks genome reactivation at the mitosis–g1 transition. Genes Dev. *30*, 1423–1439. https://doi.org/10.1101/gad.280859.116.
49. Sarnataro, S., Riba, A., and Molina, N. (2021). Regulation of transcription reactivation dynamics exiting mitosis. PLoS Comput. Biol. *17*, e1009354. https://doi.org/10.1371/journal.pcbi.1009354.
50. Krenning, L., Sonneveld, S., and Tanenbaum, M.E. (2022). Time-resolved single-cell sequencing identifies multiple waves of mrna decay during the mitosis-to-g1 phase transition. eLife *11*, e71356. https://doi.org/10.7554/elife.71356.
51. Gorin, G., Fang, M., Chari, T., and Pachter, L. (2022). Rna velocity unraveled. PLoS Comput. Biol. *18*, e1010492. https://doi.org/10.1371/journal.pcbi.1010492.
52. Nariya, M., Santiago-Algarra, D., Tassy, O., Cerciat, M., Ye, T., Riba, A., and Molina, N. (2025). Single-cell multiomics reveals the oscillatory dynamics of rna metabolism and chromatin accessibility during the cell cycle. NCBI Gene Expression Omnibus. URL: https://www.ncbi.nlm.nih.gov/geo/query/acc.cgi?acc=GSE300730 accessed: 2025-06-26.
53. Nariya, M., Santiago-Algarra, D., Tassy, O., Cerciat, M., Ye, T., Riba, A., and Molina, N. (2025). Oscillatory dynamics of mrna metabolism and chromatin accessibility in mescs during the cell cycle. Zenodo. . doi: https://doi.org/10.5281/zenodo.10462840 .
54. Arnold, P., Erb, I., Pachkov, M., Molina, N., and van Nimwegen, E. (2012). Motevo: integrated bayesian probabilistic methods for inferring regulatory sites and motifs on multiple alignments of dna sequences. Bioinformatics *28*, 487–494. https://doi.org/10.1093/bioinformatics/btr695.
55. Pachkov, M., Erb, I., Molina, N., and van Nimwegen, E. (2007). Swissregulon: a database of genome-wide annotations of regulatory sites. Nucleic Acids Res. *35*, D127–D131. https://doi.org/10.1093/nar/gkl857.

STAR★METHODS

KEY RESOURCES TABLE

REAGENT or RESOURCE	SOURCE	IDENTIFIER
Chemicals, peptides, and recombinant proteins		
DMEM (4.5g/L) w/glutamax	Gibco	10566016
Fetal bovine serum	Gibco	10270106
Sodium pyruvate	Gibco	11360070
Non-essential amino acids	Gibco	11140050
Penicillin-Streptomycin	Gibco	15140122
β-mercaptoethanol	Gibco	21985023
Leukemia inhibitory factor (LIF)	in-house	N/A
MEK inhibitor PD 0325901	Sigma Aldrich	PZ0162-5MG
GSK3 inhibitor CHIR99021	Sigma Aldrich	SML1046-5MG
Gelatine solution 0.1% in DPBS	Pan Biotec	P06-20410
Dulbecco's PBS w/o Ca and Mg	Sigma	D8637-500
Trypsine-EDTA	Gibco	25300–062
IGEPAL CA-630	Sigma Aldrich	I3021
Tris	Euromedex	EU0011
NaCl	Sigma Aldrich	S9625
MgCl2	Sigma Aldrich	208337
Tween 20	Sigma Aldrich	P1379
Digitonin	Invitrogen	BN2006
Rnase Inhibitor	Promega	N2511
BSA	New England Bio Labs	B9000S
DTT	Thermo Scientific	R0862
Flowmi cell strainer	Sigma Aldrich	BAH136800040
20X Nuclei Buffer	10X Genomics	PN-2000207
Critical commercial assays		
Chromium Next GEM Single Cell Multiome ATAC Kit A, 16 rxns	10X Genomics	PN-1000280
Chromium Next GEM Single Cell Multiome Reagent Kit A, 16 rxns	10X Genomics	PN-1000282
Library Construction Kit, 16 rxns	10X Genomics	PN-1000190
Experimental models: Cell lines		
Seeder-free mouse embryonic stem cells E14TG2a	ATCC	CRL-1821
Deposited data		
Multiome profiling of mESCs (raw)	This paper	GEO: GSE300730
Output of FourierCycle	This paper	Zenodo: https://zenodo.org/records/1046284
Interactive webserver	This paper	Webserver: https://molina.igbmc.science/FourierCycle-Home.html
Software and algorithms		
velocyto	La Manno et al.[14]	0.17.17 https://velocyto.org/velocyto.py/
scVelo	Bergen et al.[15]	0.2.2 https://scvelo.readthedocs.io/en/stable/
DeepCycle	Riba et al.[11]	https://github.com/andreariba/DeepCycle

(*Continued on next page*)

Continued

REAGENT or RESOURCE	SOURCE	IDENTIFIER
FourierCycle	This paper	https://github.com/MolinaLab-IGBMC/FourierCycle
ChromHMM	Ernst et al.[42]	https://github.com/guifengwei/ChromHMM_mESC_mm10/tree/master

EXPERIMENTAL MODEL AND STUDY PARTICIPANT DETAILS

Mouse embryonic stem (ES) cells of the E14 line (strain 129/Ola, male; S-E14TG2a) were used. Cells were authenticated by ATCC and tested negative for mycoplasma contamination. Cells were cultured feeder-free in gelatin-coated culture dishes (PAN-Biotech) using DMEM (4.5 g/L glucose w/glutamax, Gibco) supplemented with 15% of fetal bovine serum (Gibco), 1 mM sodium pyruvate (Gibco), 0.1 nM non-essential amino acids (Gibco), 100 mM β-mercaptoethanol (Gibco), 1X LIF (made in-house), 3mM CHIR99021 (Sigma Aldrich), 1 mM PD0325901 (Sigma Aldrich), and 1% penicilin-streptomycin. To maintain pluripotency, the medium was additionally supplemented with 3 μM GSK3 inhibitor CHIR99021 and 1 μM MEK inhibitor PD0325901. Cells were maintained at 37 °C in a humidified incubator with 5% CO_2. Sex-specific differences were not explicitly examined in this study and may warrant further investigation in future work.

METHOD DETAILS

Nuclei isolation

Nuclei were isolated from 4X105 mouse ES cells using 100 μL of cold lysis buffer (10 mM Tris-HCl (pH7.4), 10mM NaCl, 3 mM MgCl2, 0.1% Tween 20, 0.1% IGEPAL CA-630, 0.01% Digitonin, 1% BSA, 1mM DTT, 1 U/ μL RNase inhibitor). Cells were incubated for 5 min at 4°C, then resuspended in 1 mL chilled wash buffer (10 mM Tris-HCl (pH7.4), 10mM NaCl, 3 mM MgCl2, 0.1% Tween 20, 1% BSA, 1mM DTT, 1 U/μL RNase inhibitor) and centrifuged at 500 rcf for 5 min at 4°C. Pellet was rinsed two more times with 1 mL wash buffer, for a total of 3 washes. The nuclei pellet was resuspended in 40 μL Diluted Nuclei Buffer (1X Nuclei buffer (10X Genomics, PN-1000280), 1 mM DTT, 1 U/μL RNase inhibitor), and passed through a 40 μm Flowmi Cell Strainer (Merck).

Single nuclei library preparation and sequencing

Library preparation was performed at the GenomEast platform at the Institut de Génétique et de Biologie Moléculaire et Cellulaire. Transposition was performed using the 10X Genomics kit (PN-1000280) and nuclei were loaded into the 10X Genomics Chromium Controller with a target capture of 6,000 single nuclei. Libraries for the ATAC and 3′ mRNA were produced according to the Chromium Next GEM instructions (10X Genomics, Document CG000338 Rev F), and sequenced using the Illumina NextSeq 2000. Libraries were sequenced on an Illumina NextSeq 2000 sequencer as paired-end 28 + 85 base reads for 3′ mRNA, 50 base reads for ATAC. Image analysis and base calling were performed using RTA version 2.7.7 and BCL Convert version 3.8.4.

QUANTIFICATION AND STATISTICAL ANALYSIS

All statistical analyses were conducted using custom Python scripts, implemented in Python 3.9. The core modeling and optimization were performed using the scipy.optimize.minimize package. Model fitting and statistical model selection were conducted for each gene individually using a biophysical model of mRNA metabolism with Fourier series approximations (see STAR Methods and supplemental information).

To filter genes with oscillatory dynamics, we calculated the explained variance (r^2) of kernel-smoothed unspliced and spliced expression profiles with respect to the continuous cell cycle phase θ inferred by DeepCycle. Genes were retained for downstream analysis if $r^2 > 0.2$ in either the unspliced or spliced expression profile. In all figures, n represents the number of genes (n = 2,762 for whole cell modeling; n = 4,903 for nuclear export modeling), unless otherwise indicated.

For model fitting, we used a log-normal loss function to minimize the squared differences between predicted and observed unspliced and spliced RNA levels, with penalties to discourage overfitting and negative rate estimates (see STAR Methods). Hyperparameters λ_1 and λ_2 were selected via L-curve analysis, optimal values λ_1 = 2.0 and λ_2 = 1.5 for genome-wide inference. For rate profile plots, shaded areas denote 95% confidence intervals based on bootstrap resampling of model fits (Figures 2B and 2C). Summary statistics such as mean, median, standard deviation, and fold changes are provided in the main text and figure legends.

Model selection was performed using the Bayesian Information Criterion (BIC) to determine the best-fitting regulatory model for each gene. For this, models with different cell-cycle dependencies (transcription only, degradation only, or constant) were compared

to the full model. The number of parameters ($k = 23$ for full model, $k = 13$ for cell cycle-dependent trasncription or degradation and $k = 3$ for constant model) and data points ($N = 5,683$ cells, $N = 4,904$ nuclei) were explicitly included in the BIC calculation (Figure 2D).

For chromatin accessibility, pseudo-bulk profiles were computed by binning cells across 100 θ intervals and averaging ATAC fragment counts. Only genes with high reproducibility in chromatin accessibility across replicates (Pearson's $\rho > 0.75$) were retained.

TF footprint dynamics were calculated by aggregating Tn5 insertion events within $\pm$ 1 kb of predicted TF binding sites, identified using Motevo with 678 PWMs from SwissRegulon. Statistical significance of TF footprint changes across the cell cycle was ranked by amplitude of differential accessibility (Figure 6E).

Data processing

Raw data was processed using CellRanger (version 7.0.1), cellranger count option with the 10X reference genome mm10-2020-A, for demultiplexing, barcoded processing, and gene counting. We used velocyto (version 0.17.17, python implementation), run10x function along with the 10X reference genome to map the reads to intronic and exonic regions to obtain the unspliced and spliced quantification. We then used scVelo (version 0.2.3) for smoothing the unspliced and spiced quantifications with these hyperparameters: min_shared_counts=20, n_pcs=30, n_neighbors=30. Lastly, we ran DeepCycle on the processed data to infer the cell cycle phases.

Determining the discrete cell cycle phase transitions

DeepCycle assigns a continuous phase, θ to every cell based on their transcriptional profiles; however, out-of-the box these phases do not bear a direct correspondence to the biological events in the cell. We need to "shift" θ' s such that $\theta = 0$ corresponds to beginning of the G1 phase. For this we plotted the total mRNA counts in cells with respect to the θ, and fitted a monotonically increasing function (using radial basis functions with an exponential kernel) for 100 distinct values of θ_{shift} between $0 - 1$, we chose the value of θ_{shift} that minimizes the loss between the fit and the data, we denote this value as θ_{min} (see Figure S2). The G1/S and S/G2 transitions were determined by using gene expression values of cell cycle regulators. Since we use the same culture conditions as in Riba et al., we borrowed the values for G1/S and S/G2 transitions from this work.[11]

Filtering genes with oscillatory dynamics

We used the explained variance criterion to determine the genes that exhibit an oscillatory expression dynamics. We examined the unspliced, u, and spliced, s, levels with respect to θ, and obtained their moving averages, u^{ker} and s^{ker}, using a periodic Gaussian kernel. For every gene we calculated the explained variance r^2,

$$r_x^2 = 1 - \frac{\sum_i \left(x_i - x_i^{\text{ker}}\right)^2}{\sum_i \left(x_i - \langle x \rangle\right)^2}, \text{where } x = u, s.$$

We used a threshold of $r^2 > 0.2$ either in u or in s.

Biophysical model

e described the dynamics of the unspliced and the spliced mRNA for every gene with respect to the transcriptional phase during the cell cycle using a system of coupled ordinary differential equations,

Cell:

$$\frac{\mathrm{d}u(\theta)}{\mathrm{d}\theta} = \alpha(\theta) - \beta u(\theta)$$
$$\frac{\mathrm{d}s(\theta)}{\mathrm{d}\theta} = \beta u(\theta) - \gamma(\theta)s(\theta)$$

Nucleus:

$$\frac{\mathrm{d}u(\theta)}{\mathrm{d}\theta} = \alpha(\theta) - \beta u(\theta)$$
$$\frac{\mathrm{d}s(\theta)}{\mathrm{d}\theta} = \beta u(\theta) - \eta(\theta)s(\theta)$$

where α denotes the synthesis rate, β denotes the processing or the splicing rate, η denotes the nuclear export rate, and γ denotes the degradation rate. For every gene, we allow the synthesis, export, and degradation rates to explicitly depend on the cell cycle phase, θ. Since the dynamics in question is cyclic in nature, u, s, α , η, and γ will be periodic functions of θ. We used the Fourier approximation to solve this system of ordinary differential equations (details in supplemental information).

Model fitting

The optimization was performed using the optimize.minimize package from scipy module in python. We used loss function to be minimized was,

$$\text{Loss} = \frac{N}{2}\left[\log\sum_{i=1}^{N_{\text{cells}}}\left(u_i^{\text{obs}} - u_i^{\text{mod}}\right)^2 + \log\sum_{i=1}^{N_{\text{cells}}}\left(s_i^{\text{obs}} - s_i^{\text{mod}}\right)^2\right] + \sum_{n=1}^{N_{\text{comps}}}\left(e^{n\lambda_1}|\alpha_n|^2 + e^{n\lambda_2}|\gamma_n|^2\right) + \lambda_3\left[\sum_{i=1}^{N_{\text{bins}}}\Theta(-\alpha)\cdot\alpha^2 + \sum_{i=1}^{N_{\text{bins}}}\Theta(-\gamma)\cdot\gamma^2\right]$$

where,

u_i: observed unspliced reads in the i^{th} cell.
s_i: observed spliced reads in the i^{th} cell.
u_i^{mod}: model prediction of the unspliced reads in the i^{th} cell.
s_i^{mod}: model prediction of the spliced reads in the i^{th} cell.
α_n: Fourier coefficients for transcription rate.
γ_n: Fourier coefficients for degradation rate.
N_{cells}: total number of cells.
N_{comps}: number of Fourier components used in the series expansion $(N_{\text{comps}} = 5)$.
N_{bins}: number of θ bins, i.e., number of unique θ values $(N_{\text{bins}} = 100)$.
Θ: Heaviside theta function (to penalize negative rates).

Tuning the hyperparameters of the model

Heuristically, we found that $N_{\text{comps}} = 5$ was sufficient to capture the complex oscillatory dynamics across several genes. We penalized the model complexity by having an exponentially increasing penalties for higher frequency modes. To determine the optimal trade-off between model complexity (smaller coefficients) and data fitting (smaller residuals), we perfomed L-curve analysis. For a given gene, we scanned the 2D hyperparameter space spanned by λ_1 and λ_2. The optimal value of the λ's was the inflection point on the plot of loss versus the $\lambda \times |c_n|^2$, where $c = \alpha, \gamma, \eta$, are the Fourier coefficients (see Figure S4). We performed this analysis for select genes and found the median values of $\lambda_1^{\text{optim}} = 1.92$ and $\lambda_2^{\text{optim}} = 1.56$. We rounded these off and used $\lambda_1 = 2.0$ and $\lambda_2 = 1.5$ for all the genes.

Bayesian information criterion

For every gene that exhibited an oscillatory dynamics, we fitted alternative models – cell cycle-dependent transcription with constant degradation, cell cycle-dependent degradation with constant transcription, and constant model. For each model, we calculated the Bayesian information criterion (BIC) which is defined as,

$$\text{BIC} = k\log N - 2\log(\mathcal{L})$$

where, $\mathcal{L}$ is the maximized likelihood of the model, N is the number of data points i.e., number of cells, roughly 5000), k is the number of model parameters i.e., the number of Fourier coefficients, $k = 23$ for full model, $k = 13$ for model with constant degradation or transcription, and $k = 3$ for constant model.

Chromatin accessibility analysis

To compute chromatin accessibility dynamic profiles for each gene, we used the 10x gene annotation (Ensembl98) and extracted genomic regions from 2000 bp upstream of the TSS to the end of the gene. Then, The 10X "iscell" barcode fragments were extracted and intersected with the above genomic regions with bedtools coverage tool (v2.30.0). This resulted in two matrices, one for each replicate, containing the number of ATAC fragments mapped to each gene in every cell. Sorting cells according to their cell cycle phase, θ, and smoothing the number of ATAC fragments across cells produced chromatin accessibility profiles for each gene during the cell cycle. Only genes showing high replicate correlation ($\rho > 0.75$) between the chromatin accessibility profiles in each replicate were retained.

To determine TF footprints within accessible chromatin, we initially identified putative TF binding sites in ATAC peaks. To achieve this, we run MoteEvo[54] with a set of known Position Weight Matrices (PWMs) of 678 TFs obtained from the SwissRegulon database.[55] We then calculated TF footprints for each cell by aggregating all observed Tn5 cuts at a given distance from the predicted binding site within a window of ± 1 Kbp. Cell cycle-dependent TF footprints were computed by smoothing single-cell data sorted according to their cell cycle phase, θ. Additional smoothing along the relative genomic coordinates with respect to the TF binding sites was performed. Finally, relative TF footprints were calculated by subtracting the average TF footprint across the cell cycle.